Synthesis, Structural, and Magnetic Characterization of $YCrMnO_5$

José A. Alonso,*[a] María J. Martínez-Lope,[a] María T. Casais,[a] José L. Martínez,[a] and Vladimir Pomjakushin[b]

Keywords: Magnetic properties / Ferrimagnetic ordering / High-oxygen-pressure synthesis / Crystal structure refinement / Neutron powder diffraction / X-ray diffraction

A new oxide of nominal stoichiometry $YCrMnO_5$ has been prepared in polycrystalline form by wet-chemistry procedures followed by thermal treatments under high-oxygen-pressure conditions. This material has been characterized by X-ray and neutron powder diffraction (NPD), magnetotransport and magnetization measurements. $YCrMnO_5$ is isostructural with RMn_2O_5 oxides (R = rare earths); its crystal structure has been Rietveld refined from NPD data in the space group *Pbam*, and it contains infinite chains of $(Cr,Mn)^{4+}O_6$ octahedra sharing edges, linked together by $(Mn,Cr)^{3+}O_5$ pyramids and YO_8 units. An important level of cationic disorder has been found between both metallic sites; the refined crystallographic formula is $Y[Mn_{0.47(1)}Cr_{0.53(1)}]_{oct}$-$[Cr_{0.37(1)}Mn_{0.63(1)}]_{pyr}O_5$. The magnetic susceptibility indicates the onset of magnetic ordering below $T_c \approx 85$ K; the magnetization isotherms are characteristic of a weakly ferrimagnetic material reaching a net magnetization of 0.25 μ_B/f.u. for $H = 50$ kOe. Low-temperature NPD patterns do not exhibit any additional magnetic contribution, confirming that a long-range magnetic ordering is not fully established.

Introduction

The family of RMn_2O_5 (R = rare earths) oxides was first described in the 1960s by Bertaut et al.,[1,2] that already recognized the extraordinary flexibility of the structure with regard to the substitutions of both R and Mn atoms allowing, for instance, the preparation of $RMnTiO_5$ phases. Some RMn_2O_5 materials have recently been revisited since they are among the few oxides that show a significant magneto-ferroelectric effect,[3–7] which implies a coupling between ferroelectricity and magnetic order in the system: the application of an external magnetic field leads to the appearance of an electrical polarization. The orthorhombic crystal structure of RMn_2O_5 (space group *Pbam*) is very interesting, since it contains infinite chains of $Mn^{4+}O_6$ octahedra, linked through $[Mn^{3+}O_5]$ pyramidal units and bicapped antiprisms $[RO_8]$. The shortest metal–metal distance seen in this family is Mn1–Mn1 = 2.750(2) Å in the Nd compound. Important implications on the physical properties of these oxides can be presumed from such short distances. RMn_2O_5 compounds are antiferromagnets at low temperatures,[8] and the magnetic structures, studied from neutron diffraction data, are rather complex and incommensurate with the chemical unit cell.[9] For most of these oxides, the magnetic structure is defined by the propagation vector $k = (1/2,0,\tau)$, with τ depending on the type of R.[10,11] The ordering of the Mn ions is helicoidal, and the magnetic moments are contained on the *ab* plane. The rare-earth ions also become ordered at lower temperatures according to a sinusoidal magnetic structure. The magnetic structure was subsequently revisited for R = Er and Tb,[12] and Dy,[13] and it seems that the amplitude of the moments for the Mn ions is also modulated. Exceptionally, $BiMn_2O_5$[9,14] and $LaMn_2O_5$[15] display a commensurate magnetic arrangement, defined by the propagation vectors $k = (1/2,0,1/2)$ and $k = (0,0,1/2)$, respectively.

With the aim to induce new magnetic interactions in the members of the RMn_2O_5 family, we recently designed and prepared $YFeMnO_5$,[16] which is obtained by replacing Mn^{3+} by Fe^{3+} in YMn_2O_5. A NPD study complemented with magnetic measurements demonstrated that $YFeMnO_5$ is a ferrimagnet below $T_c \approx 165$ K, and is characterized by the propagation vector $k = 0$.[16] This is the first reported member of a novel $RFeMnO_5$ (R = rare earths) series, where Mn^{4+} occupies the octahedral positions, whereas Fe^{3+} is placed at the pyramidal sites of the structure. In this paper we report on the preparation of a new material with stoichiometry $YCrMnO_5$, which is isostructural with the RMn_2O_5 compounds and is obtained by substitution of Cr by Mn cations. This oxide must be prepared under high O_2 pressure, and it has been characterized, from the structural point of view, from NPD data, complemented with macroscopic magnetic susceptibility and transport measurements.

[a] Instituto de Ciencia de Materiales de Madrid, CSIC, Cantoblanco, 28049 Madrid, Spain
E-mail: ja.alonso@icmm.csic.es
[b] Laboratory for Neutron Scattering, ETHZ & PSI, 5232 Villigen PSI, Switzerland

Results

Preparation

$YCrMnO_5$ was obtained as a dark brown, polycrystalline powder. The preparation from the precursor powders requires the presence of moderate O_2 pressures in order to partially oxidize Mn and Cr to the tetravalent oxidation states. The presence of the competitive $YMnO_3$ perovskite, nominally containing Mn^{3+}, was minimized with thermal treatments under O_2 pressure. The final O_2 pressure is an important parameter, which was tuned after several unsuccessful trials: treatments at O_2 pressures above 55 bar led to an increase in the competitive $YCrO_4$ phase, which contains Cr^{5+}. Further, the use of finely divided and homogeneous precursors was found to be extremely important for a successful synthesis: the oxygenation process and the formation of the complex oxide are favoured by the use of reactive and homogeneous precursors. Figure 1 shows the XRD pattern of $YCrMnO_5$. It can be indexed in an orthorhombic unit cell, isotypic to RMn_2O_5, with no additional peaks that could indicate the presence of superstructures or departure from the mentioned symmetry. Minor impurities of the competitive $YMnO_3$ and $YCrO_4$ phases were always identified in the patterns.

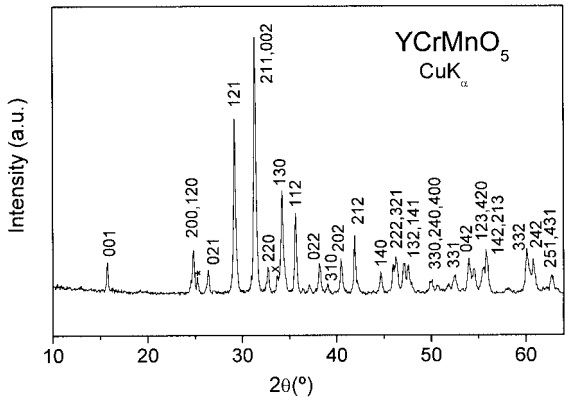

Figure 1. XRD pattern of $YCrMnO_5$, indexed in an orthorhombic unit cell with a = 7.2335(5) Å, b = 8.4953(5) Å, and c = 5.7069(4) Å. The star and the cross indicate the most intense reflections of $YCrO_4$ and $YMnO_3$, respectively.

Magnetic Measurements

The thermal variation of the *dc* susceptibility is shown in Figure 2. The magnetic susceptibility undergoes a remarkable increase below 100 K, revealing the onset of a magnetic transition at $T_C \approx 85$ K, determined from the susceptibility derivative, and an additional abrupt increment below 10 K. A linear Curie–Weiss fit in the high-temperature range 200–400 K gives a Weiss constant of $\theta_{Weiss} = -113(8)$ K, suggesting the presence of strong antiferromagnetic correlations, and an effective moment $\mu_{eff} = 5.60\ \mu_B$/f.u. In order to make clear the nature of the magnetic transitions, isothermal magnetization curves have also been measured. As can be seen in Figure 3, a hysteresis cycle is observed in the magnetization curves at 20 and 1.7 K, indicating the presence of a ferromagnetic component; in particular, at T = 1.7 K, the magnetization reaches 0.25 μ_B/formula at 50 kOe. The absence of saturation of the magnetic moments for the highest applied magnetic fields (50 kOe) is characteristic of ferrimagnetic materials or strongly canted ferromagnets. Above T_C, the magnetization curves at 150 K and 250 K present a linear behavior, corresponding to a paramagnetic state.

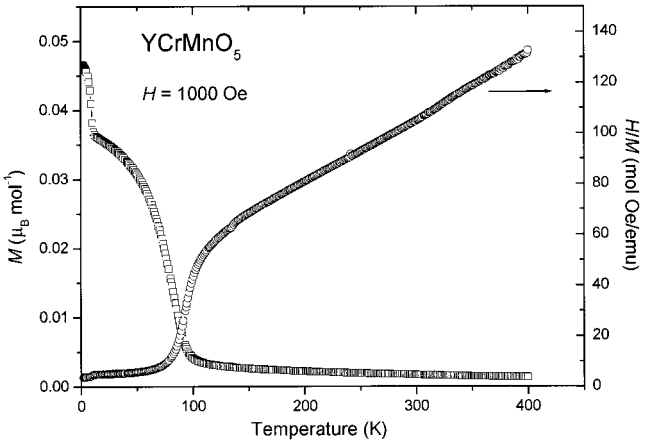

Figure 2. Thermal evolution of the magnetic susceptibility measured under a 1-kOe magnetic field. The right axis corresponds to the reciprocal susceptibility.

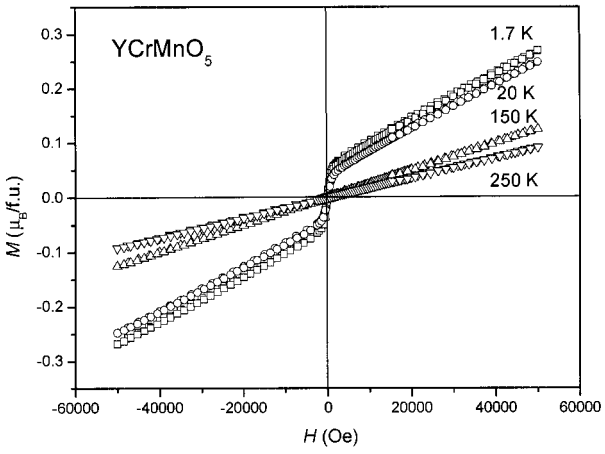

Figure 3. Isothermal magnetization curves.

Transport Properties

The temperature dependence of the electrical resistivity is shown in Figure 4. A semiconducting behavior is observed in the temperature range 160–385 K. A considerably high resistivity of $10^4\ \Omega$cm is observed at room temperature; below 160 K, the resistivity increases above $5 \times 10^6\ \Omega$cm and falls out of the measuring range of our equipment. The plot of ln ρ is linear with the reciprocal temperature, suggesting a thermally activated behavior; an Arrhenius fit gives an activation energy of 0.30 eV. The application of an external magnetic field of up to 90 kOe did not show any significant change in the resistivity, which ex-

cluded the presence of magnetoresistance in the measured temperature range, well above T_C.

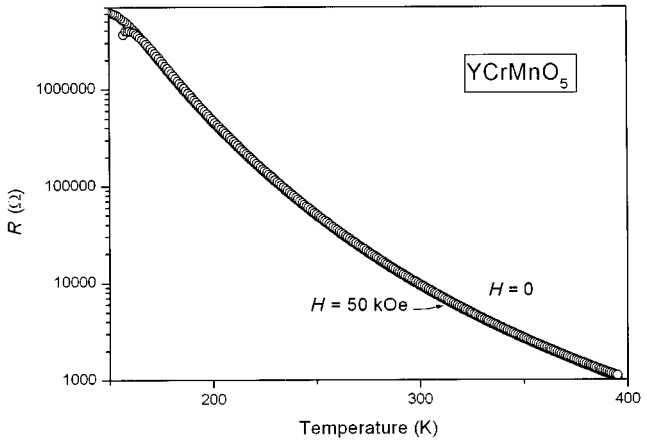

Figure 4. Thermal variation of the resistivity of $YCrMnO_5$. The curves for $H = 0$ and $H = 50$ KOe perfectly overlap.

Room-Temperature Neutron Diffraction: Crystallographic Structure

The crystallographic structure has been refined from the NPD pattern acquired at room temperature with wavelength $\lambda = 1.494$ Å. The pattern was fitted in the orthorhombic space group *Pbam*, with unit-cell parameters $a = 7.2335(5)$ Å, $b = 8.4953(5)$ Å and $c = 5.7069(4)$ Å. The crystal structure of $NdMn_2O_5$ was used as a starting model.[17,18] In the first refinement, Y atoms were placed at 4*g* (*x*,*y*,0) positions, Mn at 4*f* (0,½,*z*) sites, Cr at 4*h* (*x*,*y*,½) positions, and the four crystallographically independent oxygen atoms at 4*e* (0,0,*z*), 4*g*, 4*h* and 8*i* (*x*,*y*,*z*) positions. An unsatisfactory agreement between the calculated and observed patterns was found for this atomic distribution, leading to a discrepancy R_{Bragg} factor of 15%. The presence of antisite disorder between Cr and Mn cations was then checked; the refinement improved considerably, reaching a R_{Bragg} of 4.65%: In fact, the degree of antisite disordering was found to be extremely important in this sample, as shown in Table 1. In the final refinement, the partial occupancy of Cr/Mn at 4*f* and 4*h* positions was decoupled, allowing for the independent refinement of the occupancy factor at both sites; by doing so, the final refined stoichiometry was somewhat different to the nominal Cr/Mn = 1:1 composition, but the quality of the final refinement warrants the validity of this result. The refined crystallographic formula can be written as $Y[Mn_{0.47(1)}Cr_{0.53(1)}]_{4f}[Cr_{0.37(1)}Mn_{0.63(1)}]_{4h}O_5$, which corresponds to an empirical formula $YCr_{0.90(1)}Mn_{1.10(1)}O_5$. It is worth emphasizing that the refinement of the mixed occupancy factors of Cr and Mn over the same crystallographic site, which would be unfeasible by X-ray diffraction, is very precise by neutron diffraction given the opposite values of the scattering lengths for Cr (3.635 fm) and Mn (–3.73 fm). By the same reason, and given the comparable amounts of Cr and Mn found in both sites, the average scattering length of both sites is very weak, and the error in the determination of the corresponding positions and thermal factors is huge. As a result, in the final refinement, we fixed the positions to those determined by X-ray diffraction for both the 4*f* and 4*h* sites, and the thermal factors were fixed to 0.3 Å^2. The main structural parameters obtained in the fit are presented in Table 1. A selection of the most important atomic distances and angles is listed in Table 2. The goodness of the fit after the Rietveld refinement from the NPD data is displayed in Figure 5. The two minor impurities $YCrO_4$ (space group $I4_1/amd$, ref.[19]) and $YMnO_3$ (space group *Pbnm*, ref.[20]) were included in the refinement as second and third crystallographic phases;

Table 2. Selected interatomic distances [Å] and angles [°] for $YCrMnO_5$ at 295 K.

$(Cr,Mn)_{4f}O_6$ octahedra		YO_8	
Cr–O2 (x2)	1.973(8)	Y–O1 (x2)	2.362(5)
Cr–O3 (x2)	1.870(8)	Y–O2	2.319(6)
Cr–O4 (x2)	1.940(3)	Y–O2	2.392(6)
<Cr–O>	1.927	Y–O4 (x2)	2.337(4)
$(Mn,Cr)_{4h}O_5$ pyramids		Y–O4 (x2)	2.493(4)
Mn–O1 (x2)	1.930(7)	<Y–O>	2.387
Mn–O3	1.932(8)	Cr1–Cr1	2.96(1)
Mn–O4 (x2)	1.884(6)	Cr1–Cr1	2.74(1)
<Mn–O>	1.912	Mn2–Mn2	2.86(1)
Mn–O1–Mn	95.6(5)		
Cr–O2–Cr	97.4(14)	Cr–O3–Mn	132.0(5)
Cr–O3–Cr	94.3(7)	Cr–O4–Mn	123.0(5)

Table 1. Structural parameters after the refinement of NPD data for $YCrMnO_5$ at 295 K refined in the *Pbam* space group.

Atoms	Positions	*x*	*y*	*z*	*B* [Å^2]	Occupancy
Y	*4g*	0.1386(5)	0.1726(4)	0.00000	1.00(6)	1.0
Cr	*4f*	0.0000	0.5000	0.260(2)	0.30	0.53(1)
Mn′	*4f*	0.0000	0.5000	0.260(2)	0.30	0.47(1)
Mn	*4h*	0.4056(8)	0.3521(9)	0.50000	0.30	0.63(1)
Cr′	*4h*	0.4056(8)	0.3521(9)	0.50000	0.30	0.37(1)
O1	*4e*	0.0000	0.0000	0.2729(9)	0.98(7)	1.0
O2	*4g*	0.1678(6)	0.4444(5)	0.00000	0.41(8)	1.0
O3	*4h*	0.1534(7)	0.4270(5)	0.50000	0.75(9)	1.0
O4	*8i*	0.3918(3)	0.2088(3)	0.2487(7)	0.79(5)	1.0
Unit cell	$a = 7.2335(5)$ Å	$b = 8.4953(5)$ Å	$c = 5.7069(4)$ Å	$V = 350.69(4)$ Å^3		
Discrepancy factors	$R_p = 1.96\%$	$R_{wp} = 2.52\%$	$R_{Bragg} = 4.6\%$	$\chi^2 = 1.45$		

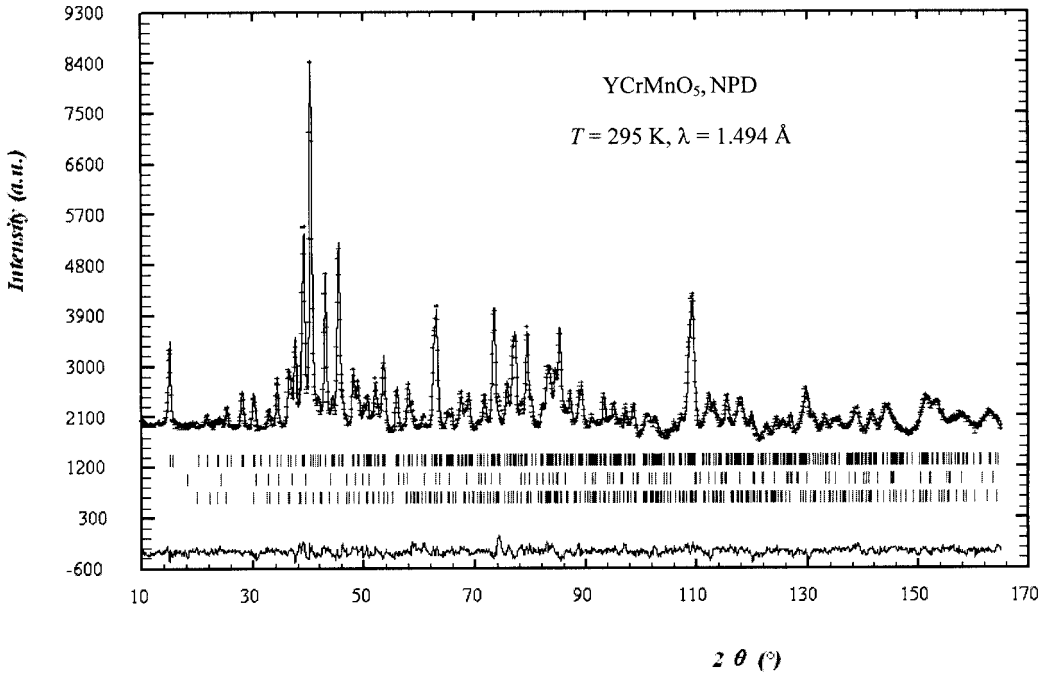

Figure 5. Observed (crosses), calculated (solid line) and difference (bottom line) NPD patterns at room temperature. The second and third series of Bragg positions correspond to the minor impurities $YCrO_4$ and $YMnO_3$, respectively.

from the scale factors, an amount of 1.34% and 2.03% of both impurities was estimated, respectively.

A view of the crystallographic structure along the *c* axis is displayed in Figure 6. There are two different oxygen environments for the atoms that occupy the 4*f* and 4*h* sites. At the 4*f* site, the $(Cr,Mn)^{4+}$ ions are inside the $M^{4+}O_6$ distorted octahedra, whereas at the 4*h* site, the $(Mn,Cr)^{3+}$ ions form $M^{3+}O_5$ distorted tetragonal pyramids. We assume that the Mn and Cr cations at the octahedral positions adopt a tetravalent oxidation state, whereas the metals at the pyramidal positions adopt a trivalent oxidation state, in order to preserve the electroneutrality of this oxide. Notice that the octahedral 4*f* positions are about half occupied by Cr and Mn, whereas the pyramidal 4*h* are about 2/3 occupied by Mn, probably because this irregular environment is well suited for the Jahn–Teller Mn^{3+} cation. The pyramids share edges to form dimer units M_2O_{10}, linked through O1 oxygen atoms. The structure contains infinite chains of $M^{4+}O_6$ octahedra, which share edges through the O2 and O3 oxygen atoms, that run along the *c* axis. The different chains of $M^{4+}O_6$ are interconnected through the M_2O_{10} pyramidal dimer units through the O3 and O4 oxygen atoms.

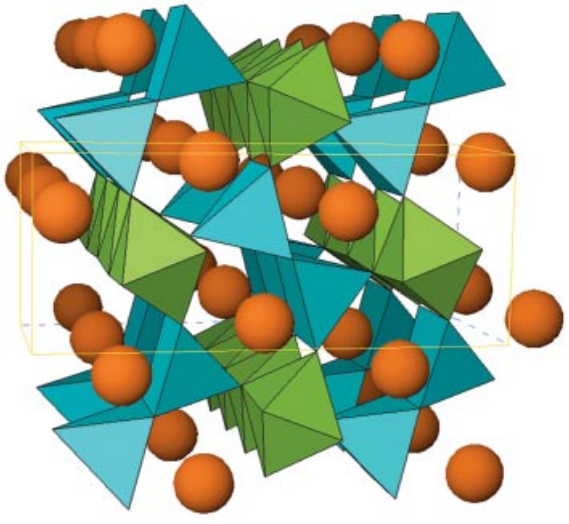

Figure 6. A view of the crystallographic structure of $YCrMnO_5$, approximately along the *c* axis. Octahedra (green) and tetragonal (turquoise) pyramids correspond to $(Cr,Mn)^{4+}O_6$ and $(Mn,Cr)^{3+}O_5$ polyhedra, respectively. Octahedra share edges, forming infinite chains along the *c* axis. Pyramids form dimer units, linking together the chains of the octahedra. Orange spheres represent the Y atoms.

Low-Temperature Neutron Diffraction Refinements

Three neutron diffraction patterns were collected below room temperature, with the hope of gaining information about the arrangement of Mn and Cr spins below the ordering temperature, T_C = 90 K. However, the low-temperature patterns collected at T = 1.5 K and 20 K did not contain any additional information, extra peaks or additional intensity on low angle Bragg reflections that could be attributed to the establishment of a long-range, ordered magnetic structure; the three patterns collected with λ = 1.886 Å could be perfectly refined by considering the crystal structure alone, with the expected shifts in unit-cell parameters and thermal factors. The upper limit of the ordered magnetic moments was determined from a simulation of a ferrimagnetic structure involving both magnetic sublattices. For the *Pbam* space group, there are two ferromagnetic Shubnikov groups: *Pb′a′m* and *Pb′am′*. The 4*f* and 4*h* sites have

Table 3. Unit cell, positional, and thermal parameters for $YCrMnO_5$, refined in the orthorhombic *Pbam* space group, from NPD data below room temperature.

T [K]	1.5	20	120
a [Å]	7.2116(6)	7.2114(6)	7.2171(5)
b [Å]	8.4970(6)	8.4963(6)	8.4953(5)
c [Å]	5.7037(4)	5.7032(4)	5.7042(4)
V [Å^3]	349.50(4)	349.44(4)	349.73(4)
Y	*4 g* (*x*,*y*,0)		
x	0.1389(5)	0.1395(5)	0.1392(5)
y	0.1720(5)	0.1711(5)	0.1714(5)
B [Å^2]	0.72(8)	0.72(8)	0.78(8)
(Mn,Cr)	*4f* (0,½,*z*)		
z	0.25972	0.25972	0.25972
B [Å^2]	0.300	0.300	0.300
(Cr,Mn)	*4h* (*x*,*y*, ½)		
x	0.40562	0.40562	0.40562
y	0.35210	0.35210	0.35210
B [Å^2]	0.300	0.300	0.300
O1	*4e* (0,0,*z*)		
z	0.274(1)	0.274(1)	0.274(1)
B [Å^2]	0.9(1)	0.8(1)	0.9(1)
O2	*4g* (*x*,*y*,0)		
x	0.1668(8)	0.1672(8)	0.1667(8)
y	0.4430(5)	4430(5)	0.4433(5)
B [Å^2]	0.2(1)	0.2(1)	0.2(1)
O3	*4h* (*x*,*y*,½)		
x	0.1557(9)	0.1551(9)	0.1548(9)
y	0.4297(6)	0.4301(6)	0.4287(6)
B [Å^2]	0.9(1)	1.1(1)	1.1(1)
O4	*8i* (*x*,*y*,*z*)		
x	0.3921(4)	0.3923(4)	0.3922(4)
y	0.2076(4)	0.2076(4)	0.2080(4)
z	0.2454(7)	0.2453(7)	0.2454(7)
B [Å^2]	0.75(8)	0.67(8)	0.64(7)
Reliability factors			
χ^2	3.71	3.57	3.07
R_{Bragg} (%)	4.82	5.03	4.93

symmetries 2 and *m*, respectively. This means that the admissible moment directions for both sites are along the *z* axis for *Pb′a′m*, and perpendicular to the *z* axis for *Pb′am′*. After trying both possibilities, the estimation for the upper limit was found to be similar in both cases, $\mu < 0.4\ \mu_B$. Table 3 lists the main structural parameters after the refinement. Figure 7 illustrates the quality of the Rietveld fit at 1.5 K; the main crystallographic phase and the two minor impurity phases, $YCrO_4$ and $YMnO_3$, are considered in the same way as those in the room temperature refinement.

Discussion

$YCrMnO_5$ is derived from the parent YMn_2O_5 oxide (containing one Mn^{3+} and one Mn^{4+} cation per formula) by full replacement of approximately half the Mn atoms by Cr atoms. The crystal structure of $YCrMnO_5$, refined from NPD data, is closely related to that of RMn_2O_5 oxides, as expected from the comparable ionic sizes for Cr^{3+} and Mn^{3+} (0.615 and 0.645 Å, respectively), and Mn^{4+} and Cr^{4+} (0.53 and 0.55 Å, respectively) in a sixfold coordination and in the high-spin state for both cations.[21] Since no structural details on the parent YMn_2O_5 have been reported, a comparison can be established with the crystal structure of $HoMn_2O_5$,[8] given the similarity in the ionic sizes of Y^{3+} (1.019 Å) and Ho^{3+} cations (1.015 Å) in an eightfold coordination.[23] In $HoMn_2O_5$ (and other RMn_2O_5 compounds), the $Mn^{4+}O_6$ octahedra are fairly flattened,[8,19] with two bonds significantly shorter than the remaining four bonds [e.g. a Mn1–O3 bond length of 1.836(8) Å for the Ho compound]; the average Mn–O distance is 1.902 Å. The same configuration is observed in $YCrMnO_5$, although

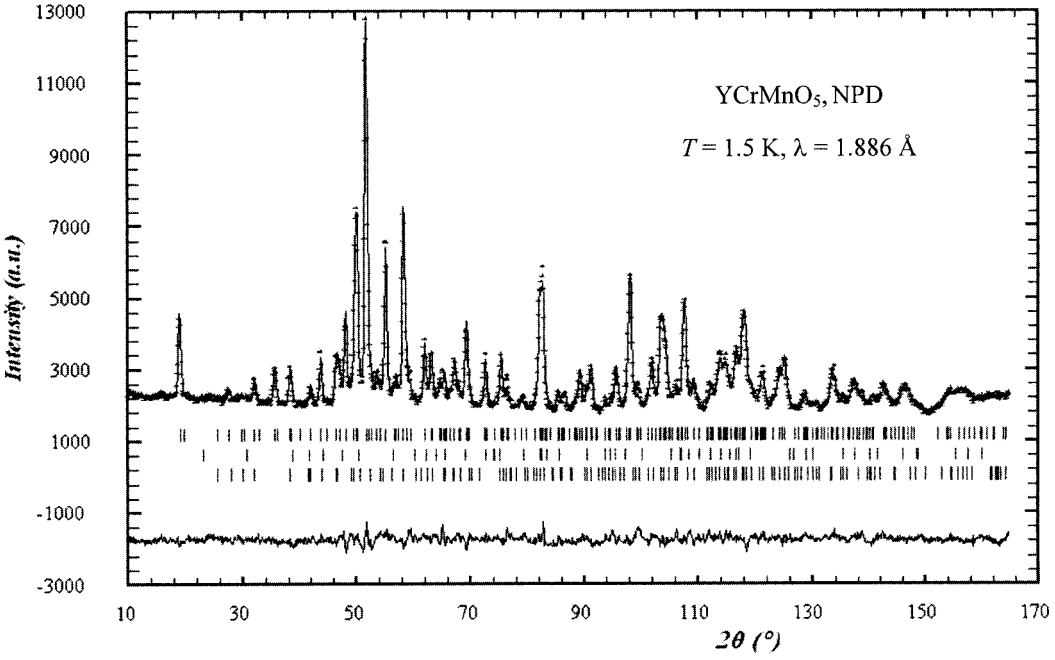

Figure 7. Observed (crosses), calculated (solid line) and difference (bottom line) NPD patterns for *T* = 1.5 K. The three series of Bragg positions correspond to $YCrMnO_5$, $YCrO_4$, and $YMnO_3$, respectively.

the individual and average $(Cr,Mn)^{4+}$–O distances are slightly longer, scaling with the greater size of Cr^{4+} cations; the average bond length is 1.927 Å. With regard to the tetragonal pyramids, $(Mn,Cr)^{3+}O_5$, the equatorial (Mn,Cr)–O1 and (Mn,Cr)–O4 bond lengths (forming the square basis of the pyramid) are similar to the corresponding Mn–O distances in the $Mn^{3+}O_5$ units of the RMn_2O_5 compounds, whereas the axial (Mn,Cr)–O3 bond length [1.932(8) Å] is shorter than that observed in $HoMn_2O_5$, where the Mn^{3+}–O3 bond in the axial position is the longest one in the $Mn^{3+}O_5$ pyramid [2.024(8) Å]. This is probably related to the Jahn–Teller character of Mn^{3+} cations, favoring an increase in the axial bond lengths in the $Mn^{3+}O_5$ pyramids, in contrast with the non-Jahn–Teller character of Cr^{4+} ($3d^5$ configuration). With respect to the oxygen coordination of the Y^{3+} cations, it can be described as $Y^{3+}O_8$ bicapped prisms, with average <Y–O> distances of 2.387 Å, which are in good agreement with the <Ho–O> bond lengths of 2.381 Å observed in $HoMn_2O_5$.

One of the most remarkable features of $YCrMnO_5$ is the high degree of antisite disordering exhibited by this compound, which implies that the octahedral positions are occupied by roughly 50% of Mn and Cr cations, and the pyramidal groups contain two thirds Mn and one third Cr cations. This feature could only be unraveled by a neutron diffraction study, thanks to the contrasting neutron scattering lengths of Cr and Mn. The trend of Cr and Mn cations sharing the same crystallographic positions is opposite to that found in $YFeMnO_5$, where a clear preference of Mn^{4+} for the octahedral positions and Fe^{3+} for the tetrahedral sites was observed.[16] The reason of this difference could be found in the relative ease of Cr vs. Fe to adopt the tetravalent oxidation state for incorporation into the octahedral positions.

The Cr/Mn antisite disordering has a dramatic influence on the magnetic properties of $YCrMnO_5$. It shows a ferromagnetic-like behavior, with $T_C \approx 85$ K and a weak magnetization at 1.7 K of 0.25 μ_B/f.u. for $H = 50$ kOe. This is reminiscent of the ferrimagnetic behavior determined for $YFeMnO_5$, which shows a superior magnetic ordering temperature of $T_C \approx 165$ K, and a saturation magnetization at low temperatures of 0.81 μ_B/formula: In $YFeMnO_5$, a NPD study demonstrated that Mn and Fe magnetic moments, at the 4*f* and 4*h* crystallographic sites of the *Pbam* space group, respectively, lie along the *z* direction and are antiferromagnetically coupled, giving rise to a global ferrimagnetic structure. Assuming a ferrimagnetic coupling between the magnetic moments at the octahedral and pyramidal positions in $YCrMnO_5$, the net magnetization could vary from zero for the hypothetical composition $YCr^{3+}Mn^{4+}O_5$ ($S = 3/2$ for Cr^{3+}; $S = 3/2$ for Mn^{4+}) to 2 μ_B/f.u. for the hypothetical $YCr^{4+}Mn^{3+}O_5$ ($S = 1$ for Cr^{4+}; $S = 2$ for Mn^{3+}) stoichiometry. Given the actual level of antisite disordering found by neutron diffraction, the net magnetization for ferrimagnetic ordering between octahedral and pyramidal positions in $Y[Mn_{0.47(1)}Cr_{0.53(1)}]_{oct}[Cr_{0.37(1)}Mn_{0.63(1)}]_{pyr}O_5$ would be of 1.16 μ_B/f.u.: This is significantly higher than that found experimentally. This fact, together with the absence of magnetic reflections in the neutron diagrams collected below T_C (at 1.5 and 20 K) demonstrate that there is only a partial long-range magnetic ordering, giving rise to ordered moments below the detection limit of the neutron diffraction technique (0.5–1 μ_B). The random occupancy of both octahedral and pyramidal positions by Cr and Mn cations hinders the establishment of a full long-range ferrimagnetic ordering between both magnetic sublattices below $T_C \approx 85$ K. For the same reason, the NPD technique does not provide any insight on the nature of the second anomaly observed in the susceptibility curve below 10 K; this probably results from a spin reorientation in the complex system, although an effect coming from the observed impurities cannot be disregarded.

Conclusions

We describe a new oxide obtained by replacing Mn by Cr in the parent YMn_2O_5 compound. The crystal structure of $YCrMnO_5$ is isotypic with that of RMn_2O_5 materials (space group *Pbam*), and contains chains of edge-linked $(Cr,Mn)^{4+}O_6$ octahedra connected by dimer groups of square pyramids $(Mn,Cr)^{3+}O_5$. A feature of the Cr compound is that the square pyramids are not elongated, showing shorter axial distances relative to the $Mn^{3+}O_5$ pyramids in RMn_2O_5. $YCrMnO_5$ is semiconducting with a large room-temperature resistivity; the magnetic susceptibility reveals the onset of a ferrimagnetic structure below $T_c \approx 85$ K. The low-temperature NPD patterns do not show any magnetic contribution, indicating that a full long-range magnetic ordering is not established down to 1.5 K, although the presence of ferrimagnetic interactions between two distinct sublattices are clearly displayed in the magnetization curves.

Experimental Section

$YCrMnO_5$ was prepared in polycrystalline form from citrate precursors obtained by a wet-chemistry procedure. Stoichiometric amounts of analytical grade Y_2O_3, $Cr(NO_3)_3{\cdot}9H_2O$, and $MnCO_3$ were dissolved in citric acid; the solution was evaporated slowly, leading to an organic resin which was dried at 120 °C and decomposed at temperatures of up to 600 °C in air. High oxygen pressure treatments were performed in a VAS furnace. About 2 g of the precursor powder was contained in a gold can during the oxygenation process. The sample was slowly heated up to 900 °C at a final pressure of 55 bar, and held at this temperature for 12 h. The product was finally cooled, under pressure, down to room temperature at 300 °C h^{-1}. Finally, the oxygen pressure was released.

The dc susceptibility measurements were performed in a commercial SQUID magnetometer. They were obtained under a 1 kOe magnetic field under field-cooling conditions and for the temperature interval $1.8 < T < 400$ K. Different isothermal magnetization curves were measured under magnetic fields ranging from –50 kOe to 50 kOe and at $T = 1.7$, 20, 150, and 250 K. Transport measurements were performed by the conventional four-probe technique in a pellet sintered under the synthesis conditions (900 °C under 55 bar O_2). Magnetotransport measurements were carried out un-

der magnetic fields of up to 90 kOe in a PPMS system from Quantum Design.

Neutron powder diffraction (NPD) diagrams were collected with the high resolution HRPT diffractometer of the SINQ spallation source, at the Paul Scherrer Institute, Villigen, Switzerland. The sample (2 g) was packed in a cylindrical vanadium holder with a 6-mm diameter. The room temperature pattern was collected with a wavelength of 1.494 Å. The sample was then cooled down in an orange cryostat, and three patterns were collected at 1.5, 20, and 120 K with a wavelength of 1.886 Å. In all cases, the high-intensity mode was used; the collection time was 4 h per diagram. The neutron diffraction patterns were analyzed with the Rietveld method,[22] using the FULLPROF program.[23] For the refinement of the profile, a pseudo-Voigt function was used to simulate the peak shape, and the background was fitted with a fifth-degree polynomial function. The coherent scattering lengths for Y, Cr, Mn, and O were, 7.75, 3.635, –3.73, and 5.803 fm, respectively. In the final run, the following parameters were refined: Background coefficients, zero-point, half-width, pseudo-Voigt, and asymmetry parameters for the peak shape; scale factor, positional, thermal factors, and unit-cell parameters.

Acknowledgments

We thank CICyT for the financial support for the project MAT2004–0479. This work was partially performed at the spallation source SINQ, Paul Scherrer Institute, Villigen, Switzerland. This research project has been supported by the European Commision under the 6th Framework Programme through the Key Action: Strengthening the European Research Area, Research Infrastructures; contract no. R113-CT-2003-505925.

[1] S. Quezel-Ambrunaz, E. F. Bertaut, G. Buisson, *C. R. Acad. Sci.* **1964**, *258*, 3025.
[2] E. F. Bertaut, G. Buisson, A. Durif, A. Mareschal, M. C. Montmory, S. Quezel-Ambrunaz, *Bull. Soc. Chim. Fr.* **1965**, 1132.
[3] A. Kadomtseva, Y. F. Popov, G. P. Vorobev, K. I. Kamilov, P. N. Makhov, M. M. Tehranchi, A. Phirouznia, *Physica B: Condensed Matter* **2003**, *329–333*, 856.
[4] K. Saito, K. Kohn, *J. Phys. Condens. Matter* **1995**, *7*, 2855.
[5] A. Inomata, K. Kohn, *J. Phys. Condens. Matter* **1996**, *8*, 2673.
[6] Y. F. Popov, A. M. Kadomtseva, S. S. Krotov, G. P. Vorob′ev, M. M. Lukina, *Ferroelectrics* **2002**, *279*, 147.
[7] Y. F. Popov, A. M. Kadomtseva, S. S. Krotov, G. P. Vorob′ev, K. I. Kamilov, M. M. Lukina, M. M. Tegranchi, *J. Exp. Theor. Phys.* **2003**, *96*, 961.
[8] J. A. Alonso, M. T. Casais, M. J. Martínez-Lope, J. L. Martínez, M. T. Fernández-Díaz, *J. Phys. Condens. Matter* **1997**, *9*, 8515.
[9] A. Muñoz, M. T. Casais, M. J. Martínez-Lope, J. L. Martínez, J. A. Alonso, M. T. Fernández-Díaz, *Phys. Rev. B* **2002**, *65*, 144423.
[10] G. Buisson, *Phys. Status Solidi A* **1973**, *16*, 533.
[11] G. Buisson, *Phys. Status Solidi A* **1973**, *17*, 191.
[12] P. P. Gardner, C. Wilkinson, J. B. Forsyth, B. M. Wanklyn, *J. Phys. C: Solid State Phys.* **1988**, *21*, 5653.
[13] C. Wilkinson, F. Sinclair, P. P. Gardner, J. B. Forsyth, B. M. Wanklyn, *J. Phys. C: Solid State* **1981**, *14*, 1671.
[14] E. F. Bertaut, G. Buisson, S. Quezel-Ambrunaz, G. Quezel, *Solid State Commun.* **1967**, *5*, 25.
[15] A. Muñoz, J. A. Alonso, M. T. Casais, M. J. Martínez-Lope, J. L. Martínez, M. T. Fernández-Díaz, *J. Mater. Chem*. 2004, in press.
[16] A. Muñoz, J. A. Alonso, M. J. Martínez-Lope, J. L. Martínez, *Chem. Mater.* **2004**, *16*, 4087.
[17] P. Euzen, P. Leone, Ch. Gueho, P. Palvadeau, *Acta Crystallogr. C* **1993**, *49*, 1875.
[18] J. A. Alonso, M. T. Casais, M. J. Martínez-Lope, I. Rasines, *J. Solid State Chem.* **1997**, *129*, 105.
[19] G. Buisson, E. F. Bertaut, J. Mareschal, *C. R. Acad. Sci.* **1964**, *259*, 411.
[20] J. A. Alonso, M. J. Martínez-Lope, M. T. Casais, M. T. Fernández-Díaz, *Inorg. Chem.* **2000**, *39*, 917.
[21] R. D. Shannon, *Acta Crystallogr., Sect. A* **1976**, *32*, 751.
[22] H. M. Rietveld, *J. Appl. Crystallogr.* **1969**, *2*, 65.
[23] J. Rodríguez-Carvajal, *Physica B* **1993**, *192*, 55.

Received: December 28, 2004

